Mon. Not. R. Astron. Soc. **000**, 1–13 (0) Printed 3 October 2011 (MN LATEX style file v2.2)

Radiative feedback on early molecular gas and implications for primordial structure formation

Margarita Petkova[1⋆], Umberto Maio[2]†
[1] *Max-Planck-Institut für Astrophysik, Karl-Schwarzschild-Straße 1, D-85748 Garching b. München, Germany*
[2] *Max-Planck-Institut für extraterrestrische Physik, Giessenbachstraße 1, D-85748 Garching b. München, Germany*

(draft)

ABSTRACT
We present results from self-consistent simulations of cosmic structure formation with a multi-frequency radiative transfer scheme and non-equilibrium molecular chemistry of e^-, H, H^+, H^-, He, He^+, He^{++}, H_2, H_2^+, D, D^+, HD, HeH^+, performed by using the simulation code GADGET. We describe our implementation and show tests for ionized sphere expansion in a static density field around a central radiative source; cosmological abundance evolution coupled with the cosmic microwave background radiation; cosmological simulations of early structure formation with radiative feedback. Our tests agree well with analytical and numerical expectations. The contributions from the detailed chemical network affect at a $\sim$ 10% level the determination of the Strömgren radius of an ionized bubble, and additional processes from the different species considered allows the gas to recombine slightly later, with respect to the H-only approximation. Moreover, we find that radiative effects from the cosmic microwave background are negligible for the mean-density evolution of different chemical species. Radiative feedback from early stars is expected to strongly lower the typical abundances of cooling molecules (e.g. H_2 and HD) up to several orders of magnitudes, hindering further gas collapse of pristine gas. This clearly suggests the relevance of metal cooling for the formation of the following generation of structures and a strong suppression of primordial population III stars.

Key words: cosmology: theory – structure formation

1 INTRODUCTION

The preset understanding of cosmic structure formation relies on the observations of a Universe expanding at a rate of $H_0 \simeq 70\,\mathrm{km/s/Mpc}$ and whose energy budget is largely dominated by a form of unknown 'dark' energy or cosmological constant, Λ, that contributes $\sim$ 70% to the total cosmic energy content. The residual matter contribution is roughly $\sim$ 30%, but only a very small fraction of $\sim$ 4% consists of ordinary baryonic matter, while the rest is unknown cold (i.e. non-relativistic) 'dark matter' (DM). More precisely, recent determinations suggest a total matter content of $\Omega_{0,\mathrm{m}} = 0.272$, $\Omega_{0,\Lambda} = 0.728$, and $\Omega_{0,\mathrm{b}} = 0.044$ (Komatsu et al. 2011). In this framework, also called ΛCDM model, cosmological structures can grow from gravitational instability (Jeans 1902) of primordial matter fluctuations, probably originated during the primordial inflationary epoch. These early perturbations represent the seeds which would develop into present-day galaxies and stars (Schwarzschild & Spitzer 1953) by gas cooling and condensation (Spitzer 1962).

Quantitatively speaking, linear perturbation analyses are usually performed to study the initial phases of gravitational collapse, where a Gaussian density distribution for the primordial matter fluctuations is assumed. The linear expansion of the continuity, Euler, and energy equations can also be extended with higher-order corrections (e.g. Tseliakhovich & Hirata 2010; Maio et al. 2011; Stacy et al. 2011; Greif et al. 2011) or non-Gaussian deviations (e.g. Grinstein & Wise 1986; Koyama et al. 1999; Komatsu et al. 2002; Grossi et al. 2007; Desjacques et al. 2009; Maio & Iannuzzi 2011), but to study non-linear regimes it is essential to perform numerical integrations and use N-body/hydro simulations. Indeed, to capture early gas collapse it is needed not only to follow gravity and hydrodynamics, but also its full chemistry evolution and molecule formation. Since in the cosmic medium hydrogen (H) is the most abundant species with a cosmological mass fraction of $X_{\mathrm{H}} \simeq 0.76$ (corresponding to $\sim$ 0.93 in number fraction), its contribution in gas cooling is likely to play a very relevant role, together with helium (He). However, H and He collisional processes are

⋆ E-mail: mpetkova@mpa-garching.mpg.de
† E-mail: umaio@mpe.mpg.de

able to cool the medium to $\sim 10^4$ K via resonant line transitions, but they are not capable to bring the gas temperature further down. At such low temperatures, thermal collisions are not able to excite the electrons to higher levels due to the large energy gaps (from a few to some tens of eV) of H and He atomic configurations. Saslaw & Zipoy (1967) proposed that gas cooling and fragmentation could be continued below $\sim 10^4$ K by H_2 cooling, down to $\sim 10^2 - 10^3$ K. Later, Lepp & Shull (1984) suggested that the existence of primordial deuterium (D) could determine HD formation and consequent cooling even below $\sim 10^2$ K, down to several ~ 10 K. During the last decades, this problems have been tackled by collecting full reaction networks (Puy et al. 1993; Galli & Palla 1998; Abel et al. 1997; Omukai et al. 2005, 2010; Glover et al. 2010) and by running high-resolution chemistry cosmological simulations, both in the standard ΛCDM model (e.g. Abel et al. 2002; Yoshida et al. 2003) and in dark-energy cosmological models (Maio et al. 2006). Further on, the effects of metal cooling have been investigated in numerical simulations by joining molecular chemistry evolution with metal pollution and low-temperature fine structure transitions from, e.g., C, O, Si, Fe (e.g. Maio et al. 2007). These studies clearly show the strong implications of metals on the cosmological chemical evolution and how the rapidity of early enrichment from first star formation episodes (see also Tornatore et al. 2007) overcomes gas molecular cooling (Maio et al. 2010, 2011), marking the transition from the primordial, pristine star formation regime - i.e. the so-called population III (popIII) regime - to the more standard population II-I (popII-I) regime (Maio et al. 2010, 2011). This transition is often parametrized in terms of a minimum critical metallicity $Z_{crit} \sim 10^{-4} Z_\odot$, but given our ignorance about early dust production and detailed atomic and molecular data, Z_{crit} has large uncertainties: its expected value varies between $\sim 10^{-6} Z_\odot$ (Schneider et al. 2003) – $10^{-5} Z_\odot$ (Omukai et al. 2010) and $\sim 10^{-3} Z_\odot$ (Bromm & Loeb 2003).

Once the first stars are formed, they shine and emit radiation. This can have relevant impacts (radiative feedback) on the surrounding medium and on the following star formation history (e.g. Ciardi et al. 2000, 2001; Shapiro et al. 2004; Whalen et al. 2004, 2010; Mellema et al. 2006; Petkova & Springel 2011; Paardekooper et al. 2011). Therefore, appropriate radiative transfer (RT) calculations coupled with hydrodynamics an chemistry must be performed in order to consistently explore the repercussions on molecule destruction or enhancement, and hence on structure formation in the early Universe. There have been studies on how the radiation feedback affects larger halos such as clusters and galaxies (e.g. Iliev et al. 2005; Yoshida et al. 2007; Croft & Altay 2008), and particular interest has arisen from popIII stars (Wise & Abel 2008; Hasegawa et al. 2009; Whalen et al. 2010), whose large luminosities not only ionize, but also expel the gas from the pristine mini-halos they sit in. For example, Lyman-Werner photons (11.2-13.6 eV) at early redshift could eradicate H_2 from halos, delaying or completely impeding the collapse of molecular gas (e.g. Wise & Abel 2007; Johnson et al. 2007; Ahn et al. 2009; Trenti & Stiavelli 2009; Whalen et al. 2010). However, several issues in this respect are still unsolved, like the role of radiative feedback on popIII star formation, its efficiency in halting gas cooling in primordial environment, its interplay with mechanical and chemical feedback, its effects on the dynamical and thermodynamical state of the cosmic gas, or its connections to the set-up of a turbulent medium dominated by hydro-instabilities (e.g. Maio et al. 2010, 2011).

In this paper, we present our technique to self-consistently combine chemistry and RT and address the effects of radiation from central sources on the nearby medium. In Sect. 2 we describe the implementations of radiation (Sect. 2.1) and chemistry evolution (Sect. 2.2). In Sect. 3, we test our implementation by performing analyses of the Strömgren sphere problem (Sect. 3.1), chemical abundance evolution (Sect. 3.2), and cosmological structure formation simulations (Sect. 3.3). We summarize, discuss and conclude in Sect. 4.

2 IMPLEMENTATIONS

We use the parallel tree N-body/SPH (smoothed particle hydrodynamics) code GADGET3, an extended version of the publicly available code GADGET2 (Springel 2005), and modify it in order to couple chemistry evolution and RT. In the following paragraphs, we give the details about the implementations of the RT (Sect. 2.1) and chemistry (Sect. 2.2) parts, and, in the next section, we will show results from our test runs.

2.1 Radiative transfer

To follow the propagation of radiation we use the implementation of RT in GADGET3 (Petkova & Springel 2009) and expand it to a multi-frequency scheme. The original implementation is based on a moment method, where the closure relation is the optically thin variable Eddington tensor, suggested by Gnedin & Abel (2001). To follow the transport of radiation, we solve the equation of anisotropic diffusion for the photon number density per frequency $n_\gamma(\nu)$:

$$\frac{\partial n_\gamma(\nu)}{\partial t} = c\frac{\partial}{\partial x_j}\left(\frac{1}{\kappa(\nu)}\frac{\partial n_\gamma(\nu) h^{ij}}{\partial x_i}\right) - c\,\kappa(\nu)\,n_\gamma(\nu) + s_\gamma(\nu), \quad (1)$$

where t is time, x_i and x_j are the coordinate components, c is the speed of light, $\kappa(\nu)$ is the absorption coefficient, h^{ij} are the components of the Eddington tensor, $s_\gamma(\nu)$ is the source function, and the Einstein summation convention is adopted for all exponents i and j.

The Eddington tensor is obtained by summing up the contributions from the sources of ionizing photons and its components are given by

$$h^{ij} = \frac{P^{ij}}{\mathrm{Tr}(P^{ij})}\,, \quad (2)$$

where

$$P^{ij}(\mathbf{x}) = \int \mathrm{d}^3x'\,\rho_*(\mathbf{x}')\frac{(\mathbf{x}-\mathbf{x}')_i(\mathbf{x}-\mathbf{x}')_j}{(\mathbf{x}-\mathbf{x}')^4} \quad (3)$$

is the radiation pressure tensor and ρ_* is the stellar density. The tensor is computed via a tree and effectively removes the dependence of the scheme on the number of ionizing sources – an advantage in cosmological and galaxy formation simulations.

The source term is treated in a *Strang-split* fashion, where photons are first "injected" into the medium surrounding the sources, and are then "diffused" via equa-

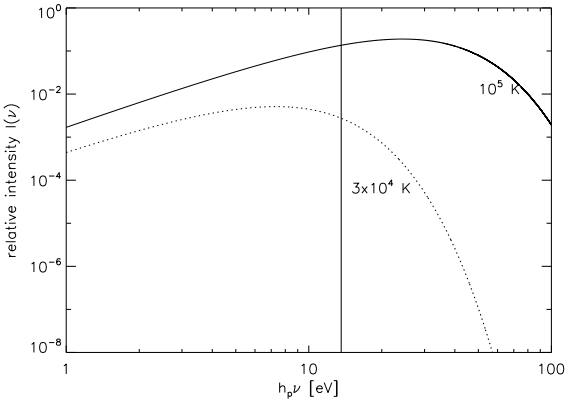

Figure 1. Intensity of a black-body spectrum as a function of photon energy in eV for two different effective temperatures - 3×10^4 K and 10^5 K. The vertical line marks the end of the Lyman-Werner band at 13.6 eV.

tion (1). Solving the equation for all particles in the simulation reduces to a linear system of equations, which we solve implicitly by using a Conjugate-Gradient scheme, that ensures robustness and stability even for large timesteps.

For our multi-frequency extension we need to transform the photon number density to ionizing intensity and vice versa. Since the photoheating and photoionization rates in equations (7) and (8) (discussed more in detail in Sect. 2.2) are obtained by integrating the intensity over frequency, we use a single photon number density in each frequency bin.

The photon number density per frequency is derived from the ionizing intensity, $I(\nu)$, as

$$n_\gamma(\nu) = \frac{1}{c}\frac{4\pi I(\nu)}{h_p\nu}\,, \tag{4}$$

where 4π is the full solid angle and h_p is the Planck constant. For any particle and at any timestep, the RT equation (1) is then solved for each frequency bin and

The intensity of the radiative source, $I(\nu)$, depends on the particular problems treated. For stellar sources, a common, simple and suitable approximation (which we will also adopt in the following) is a black-body spectrum (see Fig. 1), with effective temperature dependent on the assumed stellar population. This treatment allows us to take into account contributions from a wide frequency range, even below the H-ionization energy of 13.6 eV. Indeed, as evident from the plot in Fig. 1 the low-energy tail of the black-body spectrum contributes to the Lyman-Werner band and that will definitely affect the molecular evolution of the gas (see later).

We note that dealing with radiation below ~ 13.6 eV is a very debated and complicated problem (e.g. Thoul & Weinberg 1996; Haiman et al. 1997a,b; Omukai & Nishi 1999; Machacek et al. 2001; Kitayama et al. 2001; Ricotti et al. 2002a,b; Mackey et al. 2003; Shapiro et al. 2004; Dijkstra et al. 2004; Susa & Umemura 2004; Stacy et al. 2011), because of the many lines involved, mostly in the LW band. Full, detailed modeling of RT in such regimes is beyond the aims of this work, and, at some levels, it might be superfluous, since the ionizing flux at high redshift is dominated by radiation from neighboring haloes (Ciardi et al. 2000), rather than from the soft-UV ionizing background in the LW band.

2.2 Chemistry

To couple radiation with chemistry, we include non-equilibrium reactions for H, He and molecule evolution, by following chemical reactions (see Table 1) of several species: e^-, H, H^+, H^-, He, He^+, He^{++}, H_2, H_2^+, D, D^+, HD, HeH^+. Besides some updates in the rates and in the reaction network, the implementation used is the same as the one in Maio et al. (2007) and Maio et al. (2010) (see also Galli & Palla 1998; Abel et al. 1997). Since the main coolants at early times are H-derived molecules, H_2 (e.g. Saslaw & Zipoy 1967) and HD (e.g. Lepp & Shull 1984), the inclusion of a large network is crucial to correctly resolve the hydrodynamics and the fragmentation processes of high-redshift gas, as well demonstrated by e.g. Abel et al. (1997), Yoshida et al. (2003, 2006), Maio et al. (2006, 2007, 2009, 2010, 2011), Maio et al. (2011); Maio & Iannuzzi (2011).

To take into account chemical evolution, at each timestep and for each species i, the time variation of its number density n_i is computed, for collisional and photoionization/photodissociation events, via

$$\frac{\mathrm{d}n_i}{\mathrm{d}t} = \sum_p\sum_q k_{pq,i}n_p n_q - \sum_l k_{li}n_l n_i - k_{\gamma i}n_i, \tag{5}$$

where $k_{pq,i}$ is the rate of creation of the species i from species p and q, k_{li} is the destruction rate of the species i from collisions with species l, and $k_{\gamma i}$ is the photoionization or photodissociation rate of species i due to radiation.

The collisional rates are computed according to

$$k_{pq,i} = \int u\sigma_{pq,i}(u)f(u)\mathrm{d}^3u, \tag{6}$$

(and the analogous for k_{li}), with u relative velocity of particles p and q, $\sigma_{pq,i}(u)$ interaction cross-section, and $f(u)$ Maxwellian velocity distribution function. These rates are temperature dependent and are expressed in units of volume per time, i.e. $[\mathrm{cm}^3\,\mathrm{s}^{-1}]$ in the cgs system. As in the left-hand side, the first and second term in the right-hand side of equation (5) have dimensions of a number density per unit time, $[\mathrm{cm}^{-3}\,\mathrm{s}^{-1}]$ in the cgs system.

Consistently with Sect. 2.1, when the species i interacts with radiation (γ) – see Table 1 – and gets photoionized (like for H, D, H^-, He, He^+) or photodissociated (like for H_2, H_2^+, HeH^+), the corresponding radiative rate $k_{\gamma i}$ can be written as

$$k_{\gamma i} = \int \frac{4\pi I(\nu)}{h_p\nu}\sigma_{\gamma i}(\nu)\mathrm{d}\nu \tag{7}$$

$$= \int c\,\sigma_{\gamma i}(\nu)n_\gamma(\nu)\mathrm{d}\nu, \tag{8}$$

where the 4π stands for isotropic radiation, $I(\nu)$ is the source intensity as a function of frequency ν, $\sigma_{\gamma i}(\nu)$ is the cross-section for the given process, h_p is the Planck constant, c the speed of light, and $n_\gamma(\nu)$ the photon number density per frequency. In the final equality we made use of eq. (4), to formally get the rate expression similar to eq. (6). The radiative rates are probabilities per unit time, and are given

in [s^{-1}] in the cgs system. So, the number of radiative interactions per unit time and volume between photons and n_i particles is $k_{\gamma i} n_i$. The latter quantity is added in right-hand side of equation (5) when photon interactions are taken in consideration, and consistently with the other terms in the equation, this is also given in units of number density per time, i.e. [$cm^{-3}\,s^{-1}$] in the cgs system.

The set of differential equation (5) is integrated via simple linearization, so, given the timestep Δt, at each time t the temporal variation of the number fraction of species i can be written as

$$\frac{n_i^{t+\Delta t} - n_i^t}{\Delta t} = C_i^{t+\Delta t} - D_i^{t+\Delta t} n_i^{t+\Delta t}, \quad (9)$$

where we have introduced the creation coefficient for the species i

$$C_i = \sum_p \sum_q k_{pq,i} n_p n_q, \quad (10)$$

in [$cm^{-3}s^{-1}$], and the destruction coefficient

$$D_i = \sum_l k_{li} n_l + k_{\gamma i}, \quad (11)$$

in [s^{-1}]. The contribution from photoionization or photodissociation is accounted for by adding, in equation (11), the $k_{\gamma i}$ rates. The number density is updated from equation (9):

$$n_i^{t+\Delta t} = \frac{C_i^{t+\Delta t}\Delta t + n_i^t}{1 + D_i^{t+\Delta t}\Delta t}. \quad (12)$$

We apply this treatment to all the chemical species included, with the coefficients for each reaction in the network quoted in Table 1. Gas cooling or heating is computed from H and He collisional excitations (Black 1981; Cen 1992), ionizations (Abel et al. 1997), recombinations (Hui & Gnedin 1997), H_2 and H_2^+ emissions (Galli & Palla 1998), HD emissions (Lipovka et al. 2005), Compton effect, and Bremsstrahlung (Black 1981).

The timestepping is limited by the cooling time

$$t_{cool} = \left| \frac{E}{\dot{E}} \right| \quad (13)$$

and by the electron recombination time

$$t_e = \left| \frac{n_e}{\dot{n}_e} \right| \quad (14)$$

where E and n_e are the energy and the electron number fraction of each particle, and $\dot{E}$ and $\dot{n}_e$ the corresponding time variations. The additional constrain given by t_e is useful mostly when n_e changes very steeply, like behind the shock fronts, or at $\sim 10^4$ K, below which Hydrogen recombines very efficiently and above which Hydrogen gets ionized very fast. Further details can be found in Maio et al. (2007) and references therein.

Table 1. Reaction network

Reactions	References for the rate coefficients
$H + e^- \rightarrow H^+ + 2e^-$	A97 / Y06 / M07
$H^+ + e^- \rightarrow H + \gamma$	A97 / Y06 / M07
$H + \gamma \rightarrow H^+ + e^-$	A97 / Y06 / M07
$He + e^- \rightarrow He^+ + 2e^-$	A97 / Y06 / M07
$He^+ + e^- \rightarrow He + \gamma$	A97 / Y06 / M07
$He + \gamma \rightarrow He^+ + e^-$	A97 / Y06 / M07
$He^+ + e^- \rightarrow He^{++} + 2e^-$	A97 / Y06 / M07
$He^{++} + e^- \rightarrow He^+ + \gamma$	A97 / Y06 / M07
$He^+ + \gamma \rightarrow He^{++} + e^-$	A97 / Y06 / M07
$H + e^- \rightarrow H^- + \gamma$	GP98 / Y06 / M07
$H^- + \gamma \rightarrow H + e^-$	A97 / Y06 / M07
$H^- + H \rightarrow H_2 + e^-$	GP98 / Y06 / M07
$H + H^+ \rightarrow {H_2}^+ + \gamma$	GP98 / Y06 / M07
$H_2^+ + \gamma \rightarrow 2\,H^+ + e^-$	A97 / Y06 / M07
$H_2^+ + \gamma \rightarrow H + H^+$	A97 / Y06 / M07
${H_2}^+ + H \rightarrow H_2 + H^+$	A97 / Y06 / M07
$H_2 + H \rightarrow 3H$	A97 / M07
$H_2 + H^+ \rightarrow {H_2}^+ + H$	S04 / Y06 / M07
$H_2 + e^- \rightarrow 2H + e^-$	ST99 / GB03 / Y06 / M07
$H^- + e^- \rightarrow H + 2e^-$	A97 / Y06 / M07
$H^- + H \rightarrow 2H + e^-$	A97 / Y06 / M07
$H^- + H^+ \rightarrow 2H$	P71 / GP98 / Y06 / M07
$H^- + H^+ \rightarrow {H_2}^+ + e^-$	SK87 / Y06 / M07
${H_2}^+ + e^- \rightarrow 2H$	GP98 / Y06 / M07
${H_2}^+ + H^- \rightarrow H + H_2$	A97 / GP98 / Y06 / M07
$H_2 + \gamma \rightarrow H_2^+ + e^-$	A97 / Y06 / M07
$H_2 + \gamma \rightarrow 2\,H$	A97 / Y06 / M07
$D + H_2 \rightarrow HD + H$	WS02 / M07
$D^+ + H_2 \rightarrow HD + H^+$	WS02 / M07
$HD + H \rightarrow D + H_2$	SLP98 / M07
$HD + H^+ \rightarrow D^+ + H_2$	SLP98 / M07
$H^+ + D \rightarrow H + D^+$	S02 / M07
$H + D^+ \rightarrow H^+ + D$	S02 / M07
$D^+ + e^- \rightarrow D + \gamma$	GP98
$D + \gamma \rightarrow D^+ + e^-$	GP98
$He + H^+ \rightarrow HeH^+ + \gamma$	RD82/ GP98 / M07
$HeH^+ + H \rightarrow He + H_2^+$	KAH79 / GP98 / M07
$HeH^+ + \gamma \rightarrow He + H^+$	RD82 / GP98 / M07

Notes: γ stands for photons; P71 = Peterson et al. (1971); KAH79 = Karpas et al. (1979); RD82 = Roberge & Dalgarno (1982); SK87 = Shapiro & Kang (1987); A97 = Abel et al. (1997); GP98 = Galli & Palla (1998); SLP98 = Stancil et al. (1998); ST99 = Stibbe & Tennyson (1999); WS02 = Wang & Stancil (2002); S02 = Savin (2002); GB03 = Glover & Brand (2003); S04 = Savin et al. (2004); Y06 = Yoshida et al. (2006); M07 = Maio et al. (2007).

3 SIMULATIONS

In order to test the implementation we perform numerical simulations under different conditions. First, we numerically solve an expanding ionized sphere problem (Sect. 3.1) by fully including both the RT and chemistry treatments. Then we show the cosmic evolution of the different chemical species, coupled with the radiative gas emissions (Sect. 3.2), and finally we perform cosmological simulations of early structure formation (Sect. 3.3) to check the effects of radiative feedback on gas cooling and collapse.

For all simulations we use a set of 284 frequencies, covering the range from 0.7 eV to 100 eV. The density of frequency bins around the peaks of the photoionization and photodissociation cross-sections is increased - i.e. there are more frequency bins in the spectral regions of interest. In this way we can ensure that photons are both traced and absorbed properly and no spectrum-averaging mistakes are made.

3.1 Ionized sphere expansion

The expansion of an ionization front in a static, homogeneous and isothermal gas is the only problem in radiation hydrodynamics that has a known analytical solution and is therefore indeed the most widely used test for RT codes. For such a set-up, the ionized bubble around the ionizing source reaches a final steady radius, called the Strömgren radius, where absorptions and recombinations are balanced along the line of sight. For an H-only gas, the Strömgren radius is analytically given by

$$r_{\rm S} = \left(\frac{3\dot{N}_\gamma}{4\pi\alpha_{\rm B} n_{\rm H}^2} \right)^{1/3}, \quad (15)$$

with $\dot{N}_\gamma$ – the luminosity of the source in photons per second, $\alpha_{\rm B}$ – the case-B recombination coefficient, and $n_{\rm H}$ – the hydrogen number density. The case-B recombination coefficient assumes the so called 'on-the-spot' approximation, where photons from recombinations to lower energy levels are immediately absorbed in the vicinity of their emission (e.g. Spitzer 1978). If we approximate the ionization front (I-front) as infinitely thin, i.e. it features a discontinuity in the ionization fraction, the temporal expansion of the Strömgren radius can be solved analytically in closed form, with the I-front radius $r_{\rm I}$ given by

$$r_{\rm I} = r_{\rm S}[1 - \exp(-t/t_{\rm rec})]^{1/3}, \quad (16)$$

where

$$t_{\rm rec} = \frac{1}{n_{\rm H}\alpha_{\rm B}} \quad (17)$$

is the recombination time.

In our first test we perform an ionized sphere expansion, but we allow the temperature of the gas to vary in order to test the coupling between the RT and the full non-equilibrium chemistry treatment. As a reference, we compare to the analytical case with constant temperature. We follow the expansion of an ionized sphere around a source that emits $\dot{N}_\gamma = 5 \times 10^{48}\,\mathrm{photons\,s^{-1}}$. The shape of the source spectrum corresponds to a 3×10^4 K black body. The surrounding gas density is $\rho = 1.7 \times 10^{-27}\,\mathrm{g\,cm^{-3}}$ and is sampled by 16^3 gas particles[1]. The initial temperature of the gas is set to $T = 10^2$ K and is subject to photoheating and radiative cooling. At a temperature of 10^4 K, the case-B recombination coefficient is $\alpha_{\rm B} = 2.59 \times 10^{-13}\,\mathrm{cm^3\,s^{-1}}$. Given these parameters, the recombination time is $t_{\rm rec} = 125.127$ Myr, and the expected Strömgren radius in the isothermal (assuming $T = 10^4$ K) case is $r_{\rm S} = 5.4$ kpc.

In Fig. 2, we show the evolution of the radial position of the I-front with time. As a proxy for the position of the front we take the radius where the neutral and ionized hydrogen fractions are equal (see also Fig. 3). Our results agree within 10% with the analytical ones from equation (16).

In particular, the simple analytical solution is slightly larger than the full-simulation trend. This can naively be explained by the missing cooling contributions in the analytical calculations from, e.g., He, H_2, H_2^+, HD that lower temperatures, enhance recombination, and make the Strömgren radius decrease (as visible in the simulated case). In fact, equation (16) is computed by assuming constant temperature for hydrogen-only gas (see also Petkova & Springel 2009), while, in the numerical calculations the full chemistry treatment of Table 1, including cooling and heating, is considered.

In Fig. 3, we show the radial profile of the temperature of the gas at 500 Myr after the source has been switched on. The temperature inside the ionized region reaches several 10^4 K, consistently with photoheating from a stellar-

[1] For resolution studies, see Petkova & Springel (2009). There, it is shown that numerical convergence is reached already with 8^3 particles.

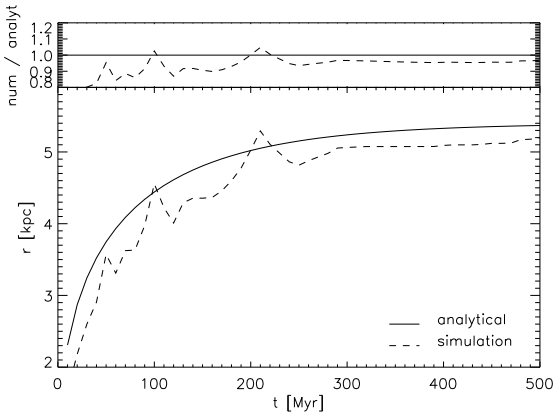

Figure 2. Evolution of the radial position of the I-front. The dashed line shows our results from the simulation, assuming the radius is at the position where the amount of neutral and ionized hydrogen is equal. The solid line is the result from the analytical equation (16). At all times the numerical result is within 10% of the analytical one, except in the beginning of the expansion.

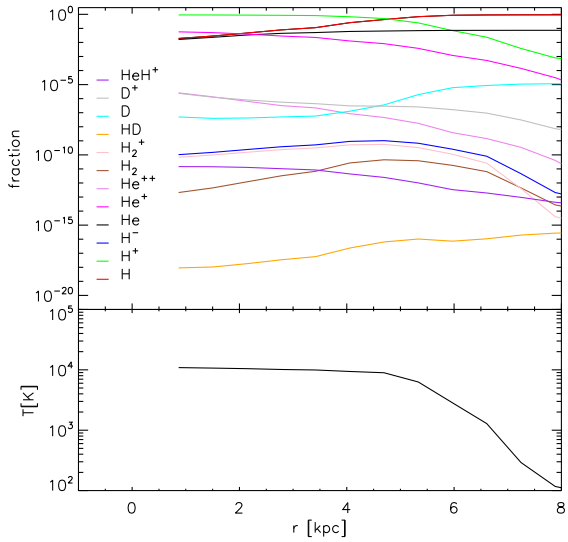

Figure 3. *Top panel*: Chemical abundance fractions radial profiles at 500 Myr after the source has been switched on. *Bottom panel*: Temperature radial profiles at 500 Myr after the source has been switched on. The temperature inside the ionized region reaches several 10^4 K and extends beyond 6 kpc since harder photons, unabsorbed by the gas, heat the medium ahead of the ionization front.

type source, and extends beyond 6 kpc – beyond the ionized region. Even further the temperature begins to drop. Harder photons (with energies > 60 eV), that do not ionize the elements effectively, heat the medium ahead of the ionization front. If the source had a harder spectrum, e.g. 10^5 K black body, than the gas would be heated even at larger radii. We stress that at a distance of > 6 kpc (namely, around the Strömgren radius) temperatures steeply drop from $\sim 10^4$ K down to $\sim 10^3$ K and recombination processes take place (see next). Correspondingly to the temperature profile, in Fig. 3, we display the radial profiles of the different chemical abundances at 500 Myr after the radiative source has been switched on. We assumed initial cosmic abundances[2], which means that hydrogen species account for $\sim 93\%$ of the total number densities and helium species for $\sim 7\%$. As expected, ionized fractions usually have larger values closer to the sources (within a few kpc), while neutral or molecular fractions increase at larger distances (above $3-6$ kpc). In the following we discuss these trends, by referring to the reaction network of Table 1, in a more precise and detailed way.

• **Atomic hydrogen species:** due to the strong radiation intensities near the central source, hydrogen is kept completely ionized (i.e. the total hydrogen fraction, ~ 0.93, is in the ionized state, H^+) within $r \lesssim 5$ kpc by the dominant photoionization process

$$H + \gamma \rightarrow H^+ + e^- . \quad (18)$$

Only at larger radii, where the radiation intensity decreases, the recombination process

$$H^+ + e^- \rightarrow H + \gamma \quad (19)$$

takes over and makes the H^+ fraction drop down of several orders of magnitude, with the consequent increase of H fraction up to ~ 0.93 (namely, the total hydrogen fraction is now in the neutral state).

H^- is a very important species because it represents one of the main channels by which molecular hydrogen can be formed (see discussion later). It shows fractional values of $\sim 10^{-9} - 10^{-10}$ until $r \lesssim 6$ kpc and at larger distances drops of roughly $3-4$ orders of magnitude. The slight increment of H^- fraction up to $\sim 10^{-9}$ in correspondence of $r \sim 4-5$ kpc is due to the simultaneous hydrogen recombination – eq. (19) – which leads to an increase of the neutral hydrogen and enhances the H^- formation via

$$H + e^- \rightarrow H^- + \gamma \quad (20)$$

reaction. In the innermost regions, photoionization

$$H^- + \gamma \rightarrow H + e^- \quad (21)$$

and collisional destruction by the abundant H^+ and e^- species

$$H^- + H^+ \rightarrow 2H \quad (22)$$

$$H^- + H^+ \rightarrow H_2 + e^- \quad (23)$$

[2] They are set to: $x_{e^-} \simeq 4 \times 10^{-4}$, $x_H = 0.926$, $x_{H^+} \simeq 4 \times 10^{-4}$, $x_{H^-} = 10^{-19}$, $x_{He} = 0.07$, $x_{He^+} = 10^{-25}$, $x_{He^{++}} = 10^{-30}$, $x_{H_2} = 10^{-13}$, $x_{H_2^+} = 10^{-18}$, $x_{HD} = 10^{-16}$, $x_D = 10^{-5}$, $x_{D^+} = 10^{-7}$, $x_{HeH^+} = 10^{-21}$.

$$H^- + e^- \rightarrow H + 2e^- \quad (24)$$

determine a lower fraction of $\sim 10^{-10}$. At larger distances ($r \sim 5 - 10$ kpc), H is dominant, but, contrary to reaction (20), free e^- are lacking and the most effective reactions are

$$H^- + H \rightarrow H_2 + e^- \quad (25)$$

$$H^- + H \rightarrow 2H + e^- \quad (26)$$

that lead to a decrease of H^- fraction down to $\lesssim 10^{-13}$.

We note that a calculation of the exact analytical expression for the the Strömgren radius and a comparison with our results is not meaningful, since the analytical study is based on the simplified case of Hydrogen-only gas and does not take into account interaction with other species and the effects of photoheating. However, the radius of the ionized hydrogen reaches ~ 5 kpc, which is approximate to the expectation value for the Strömgren radius for the isothermal case.

• **Atomic helium species:** in the same way, due to the reactions

$$He + \gamma \rightarrow He^+ + e^- \quad (27)$$

$$He + e^- \rightarrow He^+ + 2e^- \quad (28)$$

neutral He is efficiently destroyed at $r \lesssim 3$ kpc, and the residual fraction is ~ 0.01, while He^+ and He^{++} reach fractions of ~ 0.06 and $\sim 10^{-5}$, respectively, via

$$He^+ + e^- \rightarrow He^{++} + 2e^- \quad (29)$$

$$He^+ + \gamma \rightarrow He^{++} + e^- \quad (30)$$

$$He^{++} + e^- \rightarrow He^+ + \gamma \quad (31)$$

Moreover, the additional He depletion by H^+ collisions leads to the formation of HeH^+ (as we will discuss later). At $r > 3$ kpc, the decreasing intensity of ionizing radiation – which plays the most relevant role in equations (27) and (30) – and the ongoing recombination processes which take away free electrons from the medium – needed e.g. in reactions (28), (29) – cannot sustain ionization any longer and the trends exhibit monotonic radial drops for both He^+ and He^{++}. More exactly, He^+ and He recombine according to

$$He^{++} + e^- \rightarrow He^+ + \gamma \quad (32)$$

$$He^+ + e^- \rightarrow He + \gamma \quad (33)$$

respectively, so, the final states of He^+ and He^{++} are strictly linked to each other with abundances of $\sim 10^{-5}$ and 10^{-11} at $r \sim 8$ kpc. Radiative interactions are weaker and weaker and they become practically negligible at large radii.

• **Atomic deuterium species:** the behaviour of D and D^+ are quite regular and similar to H and H^+, with D^+ being dominant at $r \lesssim 5$ kpc and D dominant at $r > 5$ kpc of ~ 3 orders of magnitude. The abundances of deuterium and hydrogen species are bound by the balance reactions

$$H^+ + D \rightarrow H + D^+ \quad (34)$$

$$H + D^+ \rightarrow H^+ + D, \quad (35)$$

but the most efficient processes are still photoionization ('close' to the source)

$$D + \gamma \rightarrow D^+ + e^- \quad (36)$$

and recombination ('far' from the source)

$$D^+ + e^- \rightarrow D + \gamma. \quad (37)$$

Minor contributions of D and D^+ are also involved for molecular species (see next) and can slightly affect H or H^+ production.

• **Molecular species:** Finally, we discuss the trends of molecular species (H_2, H_2^+, HD, HeH^+). Their profiles are less regular and intuitive than atomic profiles, since more processes need to be addressed at the same time. For example, H_2 and H_2^+ have fractional values of $\sim 10^{-13}$ and $\sim 10^{-10}$, respectively, at $r \sim 1\,$kpc, then, they show an increasing trend and a peak of $\sim 10^{-10} - 10^{-9}$ at $r \sim 4-6\,$kpc. For larger r, they exhibit a drop off below $\sim 10^{-14}$, with H_2 overcoming H_2^+ at $r > 7\,$kpc. These behaviours are understood by considering that in the innermost regions the radiative negative feedback on molecule formation decreases for increasing r: this means that at larger radii radiation is not strong enough to dissociate molecules via

$$H_2 + \gamma \rightarrow 2H \quad (38)$$

and, thanks to the available H, H^+ and e^- (simultaneously present at $r \sim 4 - 6\,$kpc, where H recombination is still taking place), H_2 formation can proceed through the H^- channel – see also reaction (20),

$$H + e^- \rightarrow H^- + \gamma, \quad (39)$$

$$H^- + H \rightarrow H_2 + e^-, \quad (40)$$

and through the H_2^+ channel,

$$H + H^+ \rightarrow H_2^+ + \gamma \quad (41)$$

$$H_2^+ + H \rightarrow H_2 + H^+. \quad (42)$$

This is the intrinsic reason why molecular hydrogen roughly follows the H^- profile discussed earlier. Obviously, residual photons will slightly boost the ionized fraction of H_2^+ (with respect to H_2) via

$$H_2 + \gamma \rightarrow H_2^+ + e- \quad (43)$$

until $r \sim 7\,$kpc. At larger distances, photons are too weak to ionize the gas, so H_2 takes over and H_2^+ drops dramatically of ~ 3 orders of magnitude within 1 kpc. Additionally, we note that the sharp decrement of molecular fractions at very large distances is basically due to the fact that the medium becomes almost completely neutral and the ionized fractions of e^- and H^+ are too low to boost H^- and H_2^+, and, hence, H_2 formation.

Similarly, the increase with radius of HD fraction is essentially caused by the weakening of the central radiation and of H^+ and e^- fractions which are less and less effective in dissociating it at larger r. In particular, at $r \lesssim 4\,$kpc, H, D and H_2 are subdominant with respect to their ionized counterparts H^+, D^+ and H_2^+, thus, HD formation due to

$$D + H_2 \rightarrow HD + H \quad (44)$$

is strongly inhibited, while little contributions come from

$$D^+ + H_2 \rightarrow HD + H^+. \quad (45)$$

Destruction from reaction

$$HD + H^+ \rightarrow D^+ + H_2 \quad (46)$$

further lower HD abundances around $\sim 10^{-18}$ level. At $r \gtrsim 4$, hydrogen and deuterium recombinations, together with H_2 formation via H^- channel, support HD formation through reactions (44) and (45), instead reaction (46) is no longer effective. As a consequence, the HD fractional abundance grows more than ~ 2 orders of magnitude at $r \sim 8\,$kpc.

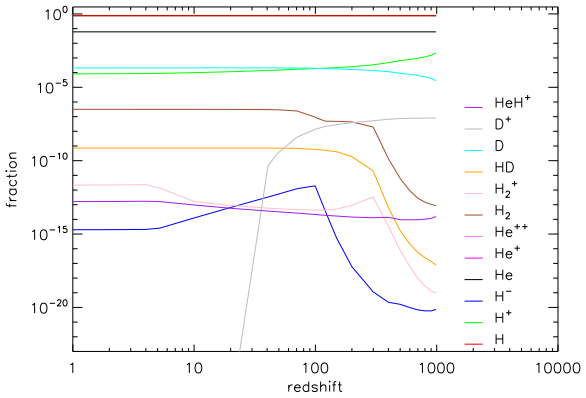

Figure 4. Number fraction evolution as a function of redshift for the different chemical species, followed in our implementation. The background cosmology is a standard flat ΛCDM model with geometrical parameters: $\Omega_{0,\rm tot} = 1.0$, $\Omega_{0,\Lambda} = 0.7$, $\Omega_{0,\rm m} = 0.3$, $\Omega_{0,\rm b} = 0.04$; spectral index $n = 1$, and spectral normalization via $\sigma_8 = 0.9$.

For what concerns the aforementioned HeH^+, this is efficiently produced near the source because there are a lot of free protons which can boost its abundance via

$$He + H^+ \rightarrow HeH^+ + \gamma \quad (47)$$

even in a more powerful way than photodissociation

$$HeH^+ + \gamma \rightarrow He + H^+. \quad (48)$$

Only when protons are lacking (i.e. at large r) HeH^+ production is inhibited up to ~ 3 orders of magnitude and drops from $\sim 10^{-11}$ to $\sim 10^{-14}$.

We stress that the residual relative ionized fractions far from the source ($r \sim 8\,$kpc) are: $n_{H^+}/n_H \sim 10^{-3}$, $n_{D^+}/n_D \sim 10^{-3}$, $n_{H^-}/n_H \sim 10^{-13}$, $n_{He^+}/n_{He} \sim 10^{-3}$, $n_{He^{++}}/n_{He} \sim 10^{-9}$, $n_{H_2^+}/n_{H_2} \sim 10^{-1}$. The absolute values quoted in the previous discussion are dependent on the initial composition assumed for the gas. Although the qualitative behaviour is not supposed to change much, larger or smaller values for the assumed fractions could result in more efficient or less efficient formation and destruction processes. However, the trends and the relative fractions of a given ionization state are expected to be quite independent from that.

3.2 Cosmological abundance evolution

In order to test how our implementation performs during cosmological evolution, we run the chemical network coupled with the RT network for the mean background density evolution and follow the changes in the different species as a function of the cosmic time. The radiative source is assumed to be the uniform CMB radiation with a black body spectrum with effective temperature of $\sim 2.73\,(1+z)\,$K. The CMB radiation is self-consistently followed, according to the

treatment outlined in Sect. 2. The initial fractions, x, for the different species[3] are initialized, at redshift $z \simeq 10^3$, accordingly to a neutral plasma at $\sim 10^3$ K (see e.g. Galli & Palla 1998).

We present the results in Fig. 4, where the cosmic mean number fractions as a function of redshift are plotted for a standard flat ΛCDM cosmology with geometrical parameters $\Omega_{0,\rm tot} = 1.0$, $\Omega_{0,\Lambda} = 0.7$, $\Omega_{0,\rm m} = 0.3$, $\Omega_{0,\rm b} = 0.04$. The H and He number fractions are unaffected by the redshift evolution.

At early times, some residual recombination process continue taking place, while the CMB temperature goes down, and make H^+ evolution drop from a fraction of $\sim 10^{-3}$, at $z \sim 1000$, to the final $\lesssim 10^{-4}$ value. The evolution of H^- clearly shows the effects of free electrons at high redshift that boost its formation (and H-derived molecule formation) from $x_{\rm H^-} \sim 10^{-20}$, at $z \sim 1000$, to $x_{\rm H^-} \sim 10^{-12}$, at $z \sim 100$. The following hydrogen recombination implies a decrease both in H^+ and e^- fraction, with consequent drop of H^- (see Table 1) down to $x_{\rm H^-} \sim 10^{-15}$ at low redshift. The two ionization states of He are constantly kept at very low values, close to the initial ones (their trends are not displayed in Fig. 4 for sake of clarity).

As already mentioned, hydrogen molecule formation is initially enhanced due to the available residual e^- and the progressively diminishing effects of CMB radiation: this allows hydrogen to increasingly form H_2^+, with a peak around $z \sim 300$, and H_2, until $z \sim 70$. H_2^+ formation is efficiently driven by H and the available H^+ in primordial times. At $z \lesssim 300$, paucity of free protons (whose fraction in the meantime has dropped of about one order of magnitude) make difficult H_2^+ formation. However, the continuous increment of H^- enhances H_2 at $z \sim 100$, and afterward its formation is mainly driven by the H^- channel, rather than the H_2^+ one, until $z \sim 70$. The dominant formation path at different times is clearly recognizable when comparing the H_2 trend with the H_2^+ and H^- trends. The $z \sim 300$ peak of H_2^+ corresponds to the steep increase of $x_{\rm H_2}$ at early times, while the $z \sim 100$ peak of H^- corresponds to the following boost at later times. For $z \lesssim 70$, $x_{\rm H_2}$ stays roughly constant between $10^{-7} - 10^{-6}$ because further production is halted by the decrement of free protons and electrons, and radiative destruction cannot take place because of the low CMB flux at low redshift.

Deuterium is also affected by cosmological evolution and the weaker CMB intensity effects at lower redshift. Thus, recombination of D and D^+ make x_D increase up to $\sim 10^{-4}$ and x_{D^+} dramatically drop down at $z < 100$. The simultaneous ongoing H_2 formation at $z \gtrsim 70$ also 'drags' HD fractions up to $\sim 10^{-9}$ levels (HD is very sensitive to H_2 abundances).

The HeH^+ molecule is often formed behind fast shocks (e.g. Neufeld & Dalgarno 1989) by He and H^+, but, due to its low dissociation energy (of $\sim 14873.6\,{\rm cm}^{-1} \sim 1.8$ eV; Bishop & Cheung 1979) it can be found and emitted only below $\sim 10^4$ K. Moreover, the presence of background radiation can dissociate it in its two components soon after the recombination epoch, at $z \lesssim 10^3$. Indeed, the plot in Fig. 4 highlights how HeH^+ is initially underabundant and then is gradually formed while the Universe expands, cools and the CMB radiation gets weaker. Over the cosmic time $x_{\rm HeH^+}$ slightly increases of one order of magnitude, from $\sim 10^{-14}$ up to $\gtrsim 10^{-13}$, and, due to H interactions, it sustains H_2^+ with subsequent H_2 formation.

The low radiation intensity of the CMB in not able to produce large changes in the abundances of the elements, but is never the less a good test on the performance of our implementation. Our results agree very well with previous cosmological abundance evolution studies as e.g. Abel et al. (1997); Galli & Palla (1998); Maio et al. (2007).

The presence of an additional cosmic UV radiation during reionization (e.g. Haardt & Madau 1996) at low redshift ($z \lesssim 7$), would heat the medium and change the ionization equilibria. As a consequence, one might expect more free electrons, larger H_2^+ and H^- abundances and hence more H_2 production, accompanied by increased D^+ and HD fractions, and dissociation of HeH^+.

3.3 Cosmological structure formation

As a final test, we present results from a cosmological structure formation simulations in the framework of the standard ΛCDM model. We use a periodical comoving box-size of $L_{\rm box} = 0.5h^{-1}$Mpc on a side with 2×64^3 gas and dark-matter particles (for a resulting spacial resolution of $\sim 0.4\,{\rm kpc}/h$ comoving), sampled at the initial redshift $z = 100$. The runs include gravity, hydrodynamics, wind feedback, non-equilibrium chemistry, and radiative transfer.

Stars are taken to be sources of ionizing radiation. Since each star particles in the simulation represents a whole stellar population with a Salpeter distribution, about 12% of its mass is in high-mass stars ($\gtrsim 10{\rm M}_\odot$) that are able to produce UV photons. The frequency distribution is assumed to be a black-body spectrum with an effective temperature of 3×10^4 K, which corresponds to a luminosity of approximately 8×10^{48} photons s^{-1} per high-mass star in the stellar population of the star particle.

We assume that gas particles are converted into stars once a critical density of $\sim 10\,{\rm cm}^{-3}$ is reached, and the gas temperature is below $\sim 10^4$K to make sure that the gas is effectively cooling (see details in Maio et al. 2009). Star forming particles also experience SN-explosion feedback, which heats the gas above $\sim 10^5$ K, and wind feedback, which expels gas with a typical velocity of ~ 500 km/s (see also Springel 2005, and references therein).

A pictorial representation of the simulated box is given in Fig. 5, where we show mass-weighted temperature slices through the simulation volume at redshift $z = 10.61$ and $z = 6.14$ for the full run, including, in particular, both non-equilibrium chemistry and RT.

The first sources are well visible close to the central part of the slice, and, while the structure growth proceeds, more sources are found in scattered places along the converging filaments. Obviously, in a wider perspective (say on ~ 100 Mpc scale), radiative source would be much more uniformly distributed. However, there are currently serious computational limitations for performing simulations with such large box sides and, simultaneously, with resolution good enough to re-

[3] They are set to: $x_{\rm e^-} \simeq 4 \times 10^{-4}$, $x_{\rm H} = 0.926$, $x_{\rm H^+} \simeq 4 \times 10^{-4}$, $x_{\rm H^-} = 10^{-19}$, $x_{\rm He} = 0.07$, $x_{\rm He^+} = 10^{-25}$, $x_{\rm He^{++}} = 10^{-30}$, $x_{\rm H_2} = 10^{-13}$, $x_{\rm H_2^+} = 10^{-18}$, $x_{\rm HD} = 10^{-16}$, $x_{\rm D} = 10^{-5}$, $x_{\rm D^+} = 10^{-7}$, $x_{\rm HeH^+} = 10^{-21}$.

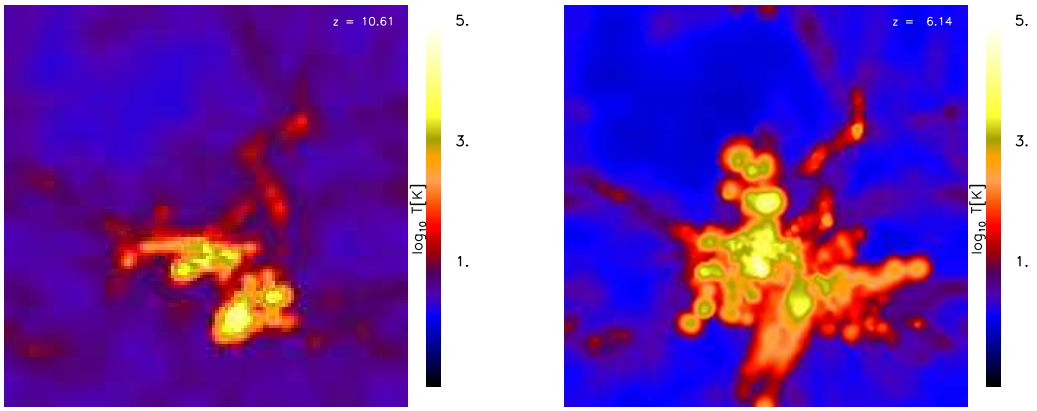

Figure 5. Mass-weighted temperature slices through the box at redshift $z = 10.61$ (left) and $z = 6.14$ (right). The simulation includes feedback effects, full non-equilibrium chemistry and RT (see text).

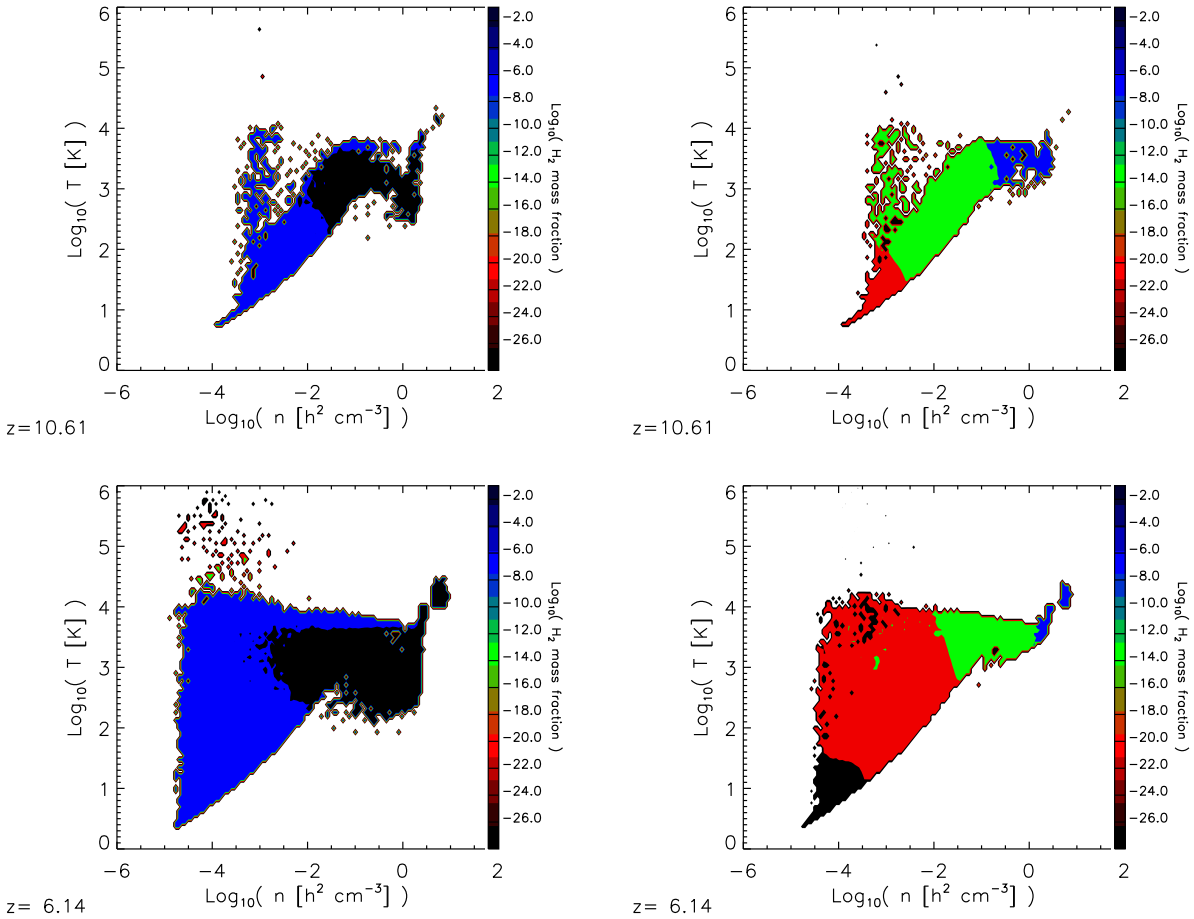

Figure 6. Phase diagrams - temperature versus gas comoving number density at redshift $z \sim 10$ (top) and redshift $z \sim 6$ (bottom) for a simulation without (left) and with (right) ionizing radiation. The color shows the mass fraction of H_2. In the presence of ionizing radiation, H_2 is depleted on all scales by many orders of magnitude. The effect is stronger at lower redshift due to the larger number of photons available.

solve chemical evolution and radiative transfer at the same time.

In the maps, the filamentary cold structures led by early molecular gas are well visible at temperatures around hundreds Kelvin. In the densest regions, radiative effects from first stars heat the medium above $\sim 10^4$ K already by redshift $z \gtrsim 10$. More and more star formation episodes appear at later stages and contribute to the cosmic reionization process down to redshift $z \simeq 6$.

Given the small size of our box, we can clearly focus on

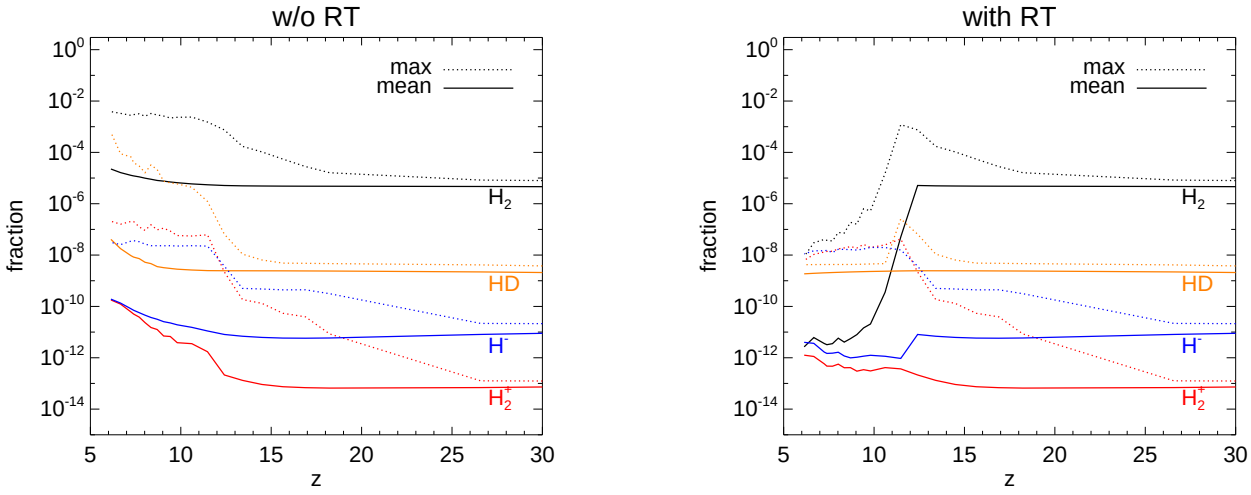

Figure 7. Evolution of the mean and maximum H_2, HD, H^- and H_2^+ fractions with redshift for the simulation with ionizing radiation (right) and without (left). When star formation sets in at redshift $z \sim 11$, the H_2 fractions drop fast, where both the mean and the maximum values are affected. The mean HD fraction stays constant in the presence of ionizing radiation and is increasing with lower redshift in the absence of radiation. The maximum follows the same trend, with the difference that it drops down as the first photos begin to propagate. There is only a small change in the evolution of the H^- fraction. Finally, the H_2^+ fraction is slightly suppressed from the ionizing radiation.

the infalling phases of the cold material in the intersection of primordial filamentary structures, and on the subsequent SN explosions, which heat the gas and push material into the lower-density, void regions. This helps understanding the different role played by the various feedback mechanisms, on the other side, the lack of a very large box also leads to an insufficient number of stellar sources to fully complete reionization by $z \sim 6$.

In Fig. 6 we plot the phase diagrams (gas temperature vs. number density) for the simulations with and without radiative treatment. The colors refer to the H_2 mass fraction. Molecular hydrogen is dissociated in the presence of ionizing radiation (mostly in the Lyman-Werner band), and this effect increases with decreasing redshift, due to the higher number of available photons. As a consequence, this lowers the star formation process, since H_2 provides the largest part of the sub-10^4 K cooling. It is evident from the plots that without radiative feedback H_2 can reach levels $\gtrsim 10^{-2}$ and boost early star formation. In presence of radiation from stellar sources, molecular fractions decrease of several orders of magnitude down to $\lesssim 10^{-5}$. This effects is much stronger for low-density gas, where molecules re-form more slowly. Such behaviour is clear from the both cases shown, at redshift $z = 10.61$ and $z = 6.14$. In the latter case, a wider temperature spread, due to thermal heating of the infalling gas at low density, appears as a consequence of the ongoing structure formation. Additionally, also SN-heated gas at $10^5 - 10^6$ K is evident with extremely low molecular fractions ($\lesssim 10^{-16}$).

The lack of cold gas in the more realistic case with both chemistry and RT suggests that low-temperature cooling by metals (e.g. Maio et al. 2007) is needed to sustain star formation after the first generation of stars (Maio et al. 2010).

To better underline the impacts of radiative effects on early chemistry, we also show in Fig. 7 the redshift evolution of the mean and maximum number fractions of the two main molecules, H_2 and HD, and of the basic species for the different channels of molecular formation, H^- and H_2^+.

As mentioned previously, after early star formation sets in, around redshift $z \sim 12$, the H_2 fractions drops by several orders of magnitude (from average values of $\sim 10^{-5}$ down to $\lesssim 10^{-10}$), as ionizing radiation starts to propagate in the simulated volume. This is not seen in the case without radiation, where H_2 increases almost monotonically, with peak values of $\sim 10^{-2}$ at $z \simeq 6$.

The mean HD fraction stays roughly constant in the presence of ionizing radiation, but it is increasing in the case without radiation. When comparing peak values, one sees that at $z \simeq 12$, HD has fractions of $\sim 10^{-6}$ in both cases, but in the RT case, it is significantly destroyed when photons begin to propagate. Instead in the non-RT case its maximum values catch up with H_2.

The H^- fraction is crucial for H_2 formation via the H^--channel: in presence of RT its mean values are lowered down to $\sim 10^{-12}$, so they cannot catalyze efficiently further molecule formation, while in the non-RT case, H^- would increase by two orders of magnitude.

Similarly, H_2^+ catalyzes H_2 formation via the H_2^+-channel, but photon propagation destroys molecules and inhibits H_2^+ formation. As a comparison, in the non-RT run H_2^+ reaches mean values of $\sim 10^{-10}$, a couple of orders of magnitude larger than in the RT run. Maximum fractions for H^- and H_2^+ are similarly suppressed of about one order of magnitude.

As a conclusion, the radiative feedback is responsible for molecule dissociation. Molecules are easily depleted not only from the external sources, but also from the central sources which have just been formed. This is justified by the fact that catastrophic molecular cooling sets in already at densities $\gtrsim 1\,\mathrm{cm}^{-3}$, when the material is optically thin, and thus there is no significant gas shielding preventing H_2 and HD dissociation. In fact, in the simulations presented here,

radiative feedback becomes effective at densities $> 10\,\mathrm{cm}^{-3}$. In the innermost central regions (i.e. below a few hundreds of comoving parsec, not sampled by our simulations because of resolution limits), densities could rise up to values greater than $\sim 10^8\,\mathrm{cm}^{-3}$, become optically thick, and produce significant shielding[4]. This should not significantly affect the overall molecular destruction over $\sim$ kpc scales by external sources, though.

4 DISCUSSION AND CONCLUSIONS

Cosmic gas and star forming processes are fundamental keywords in modern Astrophysics. They are, however, very complicated to study because they lie in the highly non-linear regime. Thus, simple perturbative approaches do not give relevant information about gas collapse and baryonic-structure growth. To understand them better, it is crucial to consider all the involved physical and chemical mechanisms. In case of early structure formation, primordial chemistry has to be taken into account, since it is mainly via H-derived molecules that first objects can aggregate gas and form stars. Furthermore, it is also necessary to self-consistently include the RT of the photons produced by stellar sources. Indeed, these travel into the cosmic medium and can ionize the surrounding gas or dissociate formed molecules. As the impacts of RT on the chemical evolution of the early Universe are expected to be significant, it is important to couple such calculations in order to get a reliable picture.

In this work, we have presented numerical studies of hydrodynamical simulations coupled with detailed chemistry treatment and multi-frequency RT. We used the SPH code GADGET3 – an extended version of the publicly available code GADGET2 (Springel 2005) – including the RT implementation of Petkova & Springel (2009), and the non-equilibrium chemistry implementation of Maio et al. (2007) , following e^-, H, H^+, H^-, He, He^+, He^{++}, H_2, H_2^+, D, D^+, HD, HeH^+.

After a detailed description of the coupling between the RT treatment (Sect. 2.1) and the non-equilibrium chemical treatment (Sect. 2.2), we have performed several tests of our code (Sect. 3).

We have started (in Sect. 3.1) with the expansion of an ionized sphere around a stellar-type source emitting at a temperature of $\sim 3 \times 10^4\,\mathrm{K}$ in a uniform-density gas. We have traced the element and molecule evolution with time and compared to analytical results (in Fig. 2 and Fig. 3). We found that analytical analyses based on H-only gas at a constant temperature give a sufficient criterion to predict the evolution of the I-front. However, full, detailed, non-equilibrium and radiative calculations show that deviations can affect the results at a $\sim 10\,\%$ level. Moreover, the different species reach different ionization radii and for reference we use only the Strömgren radius, which we have defined for H-only gas. In particular, for H_2 the ionization radius is typically larger than the Strömgren radius of about 40 per cent ($\sim 7\,\mathrm{kpc}$ vs $\sim 5\,\mathrm{kpc}$). Deuterium species recombine at a radius comparable (within 10 per cent) to the Strömgren radius, while He gets completely neutral at $\sim 2/5$ the Strömgren radius.

The second test (see Sect. 3.2) is a mean-density cosmological evolution, where the CMB was assumed to be the only source of ionizing radiation. We found that (Fig. 4), because of the low cosmic background emission, the CMB does not affect significantly the abundance evolution, even when considering photon propagation at very-high redshift.

Our final test (Sect. 3.3) has been the cosmological evolution of structure formation (e.g. Fig. 5) with and without ionizing radiation from stellar sources. We found that the presence of ionizing radiation from stars depletes molecular hydrogen up to several orders of magnitude (see Fig. 6), by inhibiting the main formation paths (the H^--channel and the H_2^+-channel) and by dissociating it via Lyman-Werner radiation. Analogous results have been recently reported by e.g. Wise & Abel (2007); Johnson et al. (2007); Ahn et al. (2009); Trenti & Stiavelli (2009); Whalen et al. (2010); Latif et al. (2011), who studied the impacts of the UV background in destroying down the H_2 molecule. In addition, we also found that other molecules formed in pristine gas like e.g. HD, are strongly suppressed by radiative feedback, as well (Fig. 7).

There are large discrepancies in the quantitative assessments of the impacts of radiative feedback on baryonic structure formation in the current literature. In fact, different works (e.g. Ciardi et al. 2000; Kitayama et al. 2001; Dijkstra et al. 2004) show uncertainties of several orders of magnitudes on the basic estimates of the masses of the haloes affected by radiation. Despite that, the negative feedback on structure formation is fairly well established.

Moreover, the destruction of early molecules by stellar sources has a deep impact on the following star formation processes, because it will hinder the successive birth of metal-free stars. This also implies the need of different viable coolants, like metals (e.g. Maio et al. 2007), in order to sustain star formation at later times. The obvious expectation is, then, that the popIII star formation rate will dramatically drop (even more heavily than expected by Maio et al. 2010, 2011; Hasegawa et al. 2009; Tornatore et al. 2007; O'Shea & Norman 2008; Johnson & Khochfar 2011) and the popII contribution will easily dominate the lower-redshift Universe.

However, further and more detailed investigations of high-resolution numerical simulations are required to draw final and definitive conclusions on this topic.

ACKNOWLEDGMENTS

The analysis and the simulations have been performed on the MPA AMD Opteron machines at the Garching Computing Center (Rechenzentrum Garching, RZG). This research has made use of NASA's Astrophysics Data System and of the JSTOR Archive.

REFERENCES

Abel T., Anninos P., Zhang Y., Norman M. L., 1997, New Astronomy, 2, 181

[4] If we consider that primordial haloes have radii of a few kpc, the fraction of volume interesting for such events is very small: for a protogalaxy having a radius of $\sim$ kpc and developing a dense core within $\sim 100\,\mathrm{pc}$, the volume fraction of high-density, possibly shielded gas is $\lesssim 10^{-3}$.

Abel T., Bryan G. L., Norman M. L., 2002, Science, 295, 93
Ahn K., Shapiro P. R., Iliev I. T., Mellema G., Pen U.-L., 2009, ApJ, 695, 1430
Bishop D. M., Cheung L. M., 1979, Journal of Molecular Spectroscopy, 75, 462
Black J. H., 1981, MNRAS, 197, 553
Bromm V., Loeb A., 2003, Nature, 425, 812
Cen R., 1992, ApJS, 78, 341
Ciardi B., Ferrara A., Abel T., 2000, ApJ, 533, 594
Ciardi B., Ferrara A., Governato F., Jenkins A., 2000, MNRAS, 314, 611
Ciardi B., Ferrara A., Marri S., Raimondo G., 2001, MNRAS, 324, 381
Croft R. A. C., Altay G., 2008, MNRAS, 388, 1501
Desjacques V., Seljak U., Iliev I. T., 2009, MNRAS, 396, 85
Dijkstra M., Haiman Z., Rees M. J., Weinberg D. H., 2004, ApJ, 601, 666
Galli D., Palla F., 1998, A&A, 335, 403
Glover S. C. O., Brand P. W. J. L., 2003, MNRAS, 340, 210
Glover S. C. O., Federrath C., Mac Low M.-M., Klessen R. S., 2010, MNRAS, 404, 2
Gnedin N. Y., Abel T., 2001, New Astronomy, 6, 437
Greif T., White S., Klessen R., Springel V., 2011, ArXiv e-prints
Grinstein B., Wise M. B., 1986, ApJ, 310, 19
Grossi M., Dolag K., Branchini E., Matarrese S., Moscardini L., 2007, MNRAS, 382, 1261
Haardt F., Madau P., 1996, ApJ, 461, 20
Haiman Z., Rees M. J., Loeb A., 1997a, ApJ, 476, 458
Haiman Z., Rees M. J., Loeb A., 1997b, ApJ, 484, 985
Hasegawa K., Umemura M., Susa H., 2009, MNRAS, 395, 1280
Hui L., Gnedin N. Y., 1997, MNRAS, 292, 27
Iliev I. T., Shapiro P. R., Raga A. C., 2005, MNRAS, 361, 405
Jeans J. H., 1902, Phil. Trans., 199, A p.1+
Johnson J. L., Greif T. H., Bromm V., 2007, ApJ, 665, 85
Johnson J. L., Khochfar S., 2011, MNRAS, 413, 1184
Karpas Z., Anicich V., Huntress Jr. W. T., 1979, J. Chem. Phys., 70, 2877
Kitayama T., Susa H., Umemura M., Ikeuchi S., 2001, MNRAS, 326, 1353
Komatsu E., Smith K. M., Dunkley J., 18 coauthors 2011, ApJS, 192, 18
Komatsu E., Wandelt B. D., Spergel D. N., Banday A. J., Górski K. M., 2002, ApJ, 566, 19
Koyama K., Soda J., Taruya A., 1999, MNRAS, 310, 1111
Latif M. A., Schleicher D. R. G., Spaans M., Zaroubi S., 2011, A&A, 532, A66+
Lepp S., Shull J. M., 1984, ApJ, 280, 465
Lipovka A., Núñez-López R., Avila-Reese V., 2005, MNRAS, 361, 850
Machacek M. E., Bryan G. L., Abel T., 2001, ApJ, 548, 509
Mackey J., Bromm V., Hernquist L., 2003, ApJ, 586, 1
Maio U., Ciardi B., Dolag K., Tornatore L., Khochfar S., 2010, MNRAS, 407, 1003
Maio U., Ciardi B., Yoshida N., Dolag K., Tornatore L., 2009, A&A, 503, 25
Maio U., Dolag K., Ciardi B., Tornatore L., 2007, MNRAS, 379, 963
Maio U., Dolag K., Meneghetti M., Moscardini L., Yoshida N., Baccigalupi C., Bartelmann M., Perrotta F., 2006, MNRAS, 373, 869
Maio U., Iannuzzi F., 2011, MNRAS, 415, 3021
Maio U., Khochfar S., Johnson J. L., Ciardi B., 2011, MNRAS, 414, 1145
Maio U., Koopmans L. V. E., Ciardi B., 2011, MNRAS, 412, L40
Mellema G., Iliev I. T., Alvarez M. A., Shapiro P. R., 2006, New Astronomy, 11, 374
Neufeld D. A., Dalgarno A., 1989, ApJ, 340, 869
Omukai K., Hosokawa T., Yoshida N., 2010, ApJ, 722, 1793
Omukai K., Nishi R., 1999, ApJ, 518, 64
Omukai K., Tsuribe T., Schneider R., Ferrara A., 2005, ApJ, 626, 627
O'Shea B. W., Norman M. L., 2008, ApJ, 673, 14
Paardekooper J.-P., Pelupessy F. I., Altay G., Kruip C. J. H., 2011, A&A, 530, A87+
Peterson J. R., Aberth W. H., Moseley J. T., Sheridan J. R., 1971, Phys. Rev. A, 3, 1651
Petkova M., Springel V., 2009, MNRAS, 396, 1383
Petkova M., Springel V., 2011, MNRAS, 412, 935
Puy D., Alecian G., Le Bourlot J., Leorat J., Pineau Des Forets G., 1993, A&A, 267, 337
Ricotti M., Gnedin N. Y., Shull J. M., 2002a, ApJ, 575, 33
Ricotti M., Gnedin N. Y., Shull J. M., 2002b, ApJ, 575, 49
Roberge W., Dalgarno A., 1982, ApJ, 255, 489
Saslaw W. C., Zipoy D., 1967, Nature, 216, 976
Savin D. W., 2002, ApJ, 566, 599
Savin D. W., Krstić P. S., Haiman Z., Stancil P. C., 2004, ApJ, 606, L167
Schneider R., Ferrara A., Salvaterra R., Omukai K., Bromm V., 2003, Nature, 422, 869
Schwarzschild M., Spitzer L., 1953, The Observatory, 73, 77
Shapiro P. R., Iliev I. T., Raga A. C., 2004, MNRAS, 348, 753
Shapiro P. R., Kang H., 1987, ApJ, 318, 32
Spitzer L., 1962, Physics of Fully Ionized Gases, New York: Interscience (2nd edition), 1962. Spitzer L.
Spitzer L., 1978, Physical processes in the interstellar medium. Spitzer, L.
Springel V., 2005, MNRAS, 364, 1105
Stacy A., Bromm V., Loeb A., 2011, ApJ, 730, L1+
Stacy A., Greif T. H., Bromm V., 2011, ArXiv e-prints
Stancil P. C., Lepp S., Dalgarno A., 1998, ApJ, 509, 1
Stibbe D. T., Tennyson J., 1999, ApJ, 513, L147
Susa H., Umemura M., 2004, ApJ, 600, 1
Thoul A. A., Weinberg D. H., 1996, ApJ, 465, 608
Tornatore L., Ferrara A., Schneider R., 2007, MNRAS, 382, 945
Trenti M., Stiavelli M., 2009, ApJ, 694, 879
Tseliakhovich D., Hirata C., 2010, Phys. Rev. D, 82, 083520
Wang J. G., Stancil P. C., 2002, Physica Scripta, T96, 1, 72
Whalen D., Abel T., Norman M. L., 2004, ApJ, 610, 14
Whalen D., Hueckstaedt R. M., McConkie T. O., 2010, ApJ, 712, 101
Wise J. H., Abel T., 2007, ApJ, 671, 1559
Wise J. H., Abel T., 2008, ApJ, 685, 40

Yoshida N., Abel T., Hernquist L., Sugiyama N., 2003, ApJ, 592, 645
Yoshida N., Oh S. P., Kitayama T., Hernquist L., 2006, ArXiv Astrophysics e-prints
Yoshida N., Oh S. P., Kitayama T., Hernquist L., 2007, ApJ, 663, 687
Yoshida N., Omukai K., Hernquist L., Abel T., 2006, ApJ, 652, 6